Prediction of Crystallinity for Large-Scale Additive Manufacturing with Complex Temperature Histories

Y.T. Schäfer[1*], A.R. Chadwick[1]

[1] German Aerospace Centre (DLR), Institute of Structures and Design, Stuttgart, Germany

* *Corresponding author (yannick.schaefer@dlr.de)*

Keywords: *LM-PAEK; Crystallization Kinetics; Process Simulation; DSC; 3D-Printing*

1. Abstract

The introduction of additive manufacturing techniques using material extrusion may provide a means of bonding stiffening structures onto thermoplastic composite skins in-situ, offering a reduction in complexity, cost and lead time. Aerospace-grade semi-crystalline polymers, however, are difficult to process using these such techniques, largely owing the complex temperature histories and the crystallization behaviour affecting the diffusion bonding. In this paper, a Nakamura-based crystallization model for the new material grade 231GRA of short-fibre reinforced LM-PAEK is derived by means of re-fitting a published model for the similar TC1225 prepreg and introducing a new induction sub-model. Complex temperature histories are extracted from real printed structures with an infrared camera, and the final part crystallinity value is determined from DSC. The crystallinity simulation shows great sensitivity to the selection of emissivity, but matches the experimental values with some offset.

2. Introduction

Thermoplastic composites are widely utilised in aircraft structures and are increasingly popular owing to their low-energy storage properties, high fracture toughness, and weldability. At present, thermoplastics are restricted to small-scale, secondary structure functions not because they lack the necessary mechanical performance, but because the complexities of semi-crystalline polymers (crystallization, shrinkage, warpage, and large temperature gradients) make the conventional trial-and-error development process of new parts prohibitively expensive [1]. Aside from the conventional processing methods, the melt and re-solidification properties of thermoplastics allows for additive manufacturing such as Automated Fibre Placement (AFP) with continuous fibre reinforcement and Material Extrusion (MEX) for neat polymer and short fibre reinforced material. Additive manufacturing is typically associated with high cooling rates, resulting from the rapid deposition of small volumes of heated material in contrast to the comparatively slower heating and cooling in conventional bulk consolidation processes. The use of elevated ambient or tool temperatures is common in Fused Filament Fabrication (FFF) and AFP, respectively, to achieve a reduction in warpage and increase in performance by decreasing the temperature differentials and thus reducing cooling rates [2, 3]. AFP is typically used for manufacturing of thin laminates, where a heated tool can affect the entire structure. Fused Granulate Fabrication (FGF),

on the other hand, is typically used to manufacture out-of-plane structures, thus limiting the effect of a heated tool to the first few layers. For thin structures like single-walled stiffening elements, the cooling rate is further increased by the large fraction of surface exposed to ambient conditions in the robotic cell.

The manufactured part quality, which may be assessed in terms strength and warpage, depends in all thermoplastic manufacturing processes to a large degree on the thermal history influencing the molecular bonding and shrinkage behaviour [4, 5]. This is particularly dominant for semi-crystalline material, where the onset of crystallization inhibits further molecular diffusion [6, 5] and is associated with volumetric shrinkage and an increase in elastic modulus, both driving residual stresses [7].

The cooling rates in MEX processes, depending on the geometry and processing parameters, can become high enough to prevent crystallization altogether. Subsequent energy inputs, for example from the thermal mass of subsequent layers in an additive process, may lead to cold crystallization at much lower temperatures, close to the glass transition. A crystallization model suitable for additive manufacturing must therefore account for this temperature regime and be valid for multiple cycles of crystallization acceleration and deceleration.

Crystallization has been studied extensively over the last several decades. Modelling approaches for the crystallization kinetics can be broadly categorised into physical mathematical modelling descriptions and model-free empirical approaches. Physical models seek to describe the underlying mechanisms of nucleation and growth, with the Avrami model being foundational to the field. Nakamura et al. extended this framework to non-isothermal conditions via an isokinetic assumption [8]. Gordnian proposed a rate-type formulation in which crystallinity evolution is governed by a differential equation dependent on current state variables alone, rather than the accumulated thermal history, rendering it applicable to the complex, non-monotonic temperature cycles characteristic of thermoplastic composite manufacturing [9]. Empirical approaches such as this forgo physical interpretation and instead fit mathematical functions directly to experimentally measured crystallinity data, offering simplicity and accuracy for one specific material. Physical mathematical models may not provide the highest level of accuracy as desired for process engineering, but are attractive due to their descriptive formulation and therefore manipulability.

This work is built around a new grade of pellets for MEX, that is 30% short carbon fibre-reinforced Low-Melting Poly-Aryl-Ether-Ketone (LM-PAEK). As available literature does not provide any information on the crystallization kinetics of this specific material, this work attempts to derive a crystallization model for the fast-track estimation of additive processes, avoiding the prohibitively large financial and time effort required for the development of a completely new data driven model.

Bentalib et al. [10] recently published a Nakamura-based model for TC1225, which is a closely related LM-PAEK prepreg with 60% fibre fraction, providing all the necessary equations and fitting parameters. Within this work, we modify these equations by re-fitting parameters that are expected to vary with the fibre fraction and the addition of a new, low test effort induction model. Experimental validation of the model is done with 3D-printed samples with corresponding temperature histories extracted using infrared camera measurements.

3. Materials and Methodology

3.1. Materials and Instrumentation

Additive manufacturing-grade short fibre reinforced LM-PAEK pellets 231GRA were sourced from Victrex Europa GmbH. This material is in a late development stage and currently the only available short fibre reinforced LM-PAEK material.

The crystallinity was measured with a NETZSCH DSC 214 Polyma Differential Scanning Calorimeter (DSC). Samples of 5-10 mg were prepared in aluminium crucibles with pierced lids. The enthalpy of crystallization and melt were determined from 10 °C/min heating ramps (in a nitrogen atmosphere) up to 360 °C. Crystallinity was calculated with equation (1) with the enthalpy of melt H_m and enthalpy of crystallization H_c. The reference enthalpy H_{ref} of 130 J/g was taken from literature [11], and the fibre mass fraction w_f of 0.299 from the manufacturers laboratory report.

$$X_c = \frac{|H_m| - |H_c|}{H_{ref}(1 - w_f)} \tag{1}$$

Part temperatures during printing were determined from infrared camera (IR) measurements using a FLIR A8302sc camera recording at 60 Hz with a 50 mm lens and an emissivity of 1.0[1]. The camera was positioned perpendicular to the part, resulting in a 4.5 pixel per mm image resolution in both axes. The quasi-static melt extrusion temperature was recorded using a 250 µm type K thermocouple inserted into the nozzle during extrusion.

The FGF process was carried out with a robot-mounted Weber DXR 25 single screw extruder equipped with a 2 mm round, blunt tip nozzle. The printed geometry features two straight paths of 170 mm length, transitioning tangentially into 25 mm radius turns which results in a layer length of 497 mm. The part was sliced with a layer height of 0.5 mm, and extrusion was adjusted to result in approximately 3 mm wide beads. Printing speeds of 45, 39, 30 and 21 mm/s were chosen for the experimental section of this work, because they were known to result in high to low crystallinities, respectively, when combined with this specific layer length.

3.2. Analytical Discussion of the Temperature Distribution

Given that the IR camera will only measure the surface temperature of the structure, the Biot number was estimated using equation (2) to assess the through thickness temperature gradient of the printed wall at a representative temperature of 200°C.

$$Bi = \frac{h_{conv}}{k} \cdot L \tag{2}$$

The convective heat transfer coefficient h_{conv} is assumed to $10 \frac{\mathrm{W}}{\mathrm{m^2K}}$ given the case of natural convection with still air in the robot cell and a relatively small structure. The thermal conductivity

[1] Previous experiments with the same material and printing setup, but with an IR camera of higher resolution indicated that an emissivity in the range of 0.95 to 1.0 would be required to match the extrusion temperature of 361°C. See section 5 for further discussion

k is unknown for the 231GRA material. Instead, the value of approximately $0.5\,\frac{\mathrm{W}}{\mathrm{mK}}$ for 30% short carbon fibre reinforced PEEK in transverse direction at 200°C was taken from Choy et al. [12]. Here, the length L is the half wall thickness of 1.5 mm. The effect of radiation is considered according to Bergman [13] by including the radiation heat transfer coefficient resulting in an effective heat transfer coefficient as in equation (3) with the ambient and wall temperatures of $T_{amb} = 293$ K and $T_{wall} = 473$ K, respectively, and the emissivity ϵ and Boltzmann's constant σ.

$$h_{eff} = h_{conv} + \epsilon\sigma(T_{amb} + T_{wall})(T_{amb}^2 + T_{wall}^2) = 23.4\,\frac{\mathrm{W}}{\mathrm{m^2K}} \tag{3}$$

The resulting Biot number of 0.07 is lower than 0.1, therefore, we can assume a nearly uniform temperature across the thickness of the printed wall and consider the surface temperature equal to the bulk temperature.

3.3. *Induction Modelling*

Induction time is commonly studied under isothermal conditions. The delay of the onset of crystallization can be described with equation (4) taken from Chan and Isayev [14].

$$t_i = t_m(T_m^0 - T)^{-a} \tag{4}$$

Here, t_i is the induction time at any isothermal temperature T, with material constant fitting parameters t_m, a, and the reference temperature T_m^0. The transfer of isothermal kinetics to non-isothermal, transient temperature histories is approached following Silfleet et al. [15]. The isokinetic method predicts that induction is additive and follows equation (5) with the onset of crystallization at time t_2 after t_1 when the integral over the isothermal induction times $t_i(T)$, that is equation (4), equals 1.

$$t_{i,transient} = \int_{t_1}^{t_2} \frac{dt}{t_{i,isothermal}\,(T)} = 1 \tag{5}$$

Fitting is most conveniently done from isothermal DSC tests. However, the limited cooling rates available using a conventional DSC and the increasing speed of induction at lower temperatures resulted, for most isothermal temperatures, in induction prior to equilibration of the enthalpy peak associated with the change from cooling to isothermal hold. Therefore, an approach was used for fitting to induction times at constant cooling rates under the assumption that equations (4) and (5) are valid. This has the advantage that the DSC temperature control induced enthalpy overshoot takes place in the melt region where it does not overlay with the induction time measurement, rather than at the beginning of an isothermal hold. Tests were conducted at constant cooling rates ϕ (treated as negative heating rates), which can be analytically described and integrated with eqations (4) and (5). The temperature profile starting from a reference temperature T_m^0, that is the lowest temperature at which crystallization would not occur, is

$$T = T_m^0 + \phi t \tag{6}$$

The instantaneous induction for this case becomes

$$t_i = t_m\left(T_m^0 - (T_m^0 + \phi t)\right)^{-a} = t_m(-\phi t)^{-a} \tag{7}$$

and thus, the total induction at onset is

$$\int_0^{t_i} \frac{1}{t_m(-t\phi)^{-a}}\,dt = \frac{(-\phi)^a}{t_m}\int_0^{t_i} t^a dt = 1 \tag{8}$$

which can be analytically solved to

$$t_i = [t_m(a+1)]^{\frac{1}{a+1}} \cdot (-\phi)^{-\frac{a}{a+1}} \tag{9}$$

This solution is of course dependent on the choice of reference temperature, driving the absolute values of DSC measured transient induction time.

Tests were conducted on 6 samples each, cooling at 1, 5, 10, 15 and 20°C/min from 360°C. The arbitrary reference temperature problem is addressed by adding a set of 6 isothermal tests at 295°C (providing both slow induction and a distinct enthalpy of crystallization), reached by a cooling ramp of 200°C/min, to the fitting database. The onset of crystallization was determined as the time at which 0.01% crystallinity is reached. Fitting was performed with the curve fit toolbox in python with an initial value of $T_m^0 = 304°C$.

3.4. Crystallization Modelling

The model used in this paper is based on the work of Bentalib et al., with the addition of the induction model discussed above. It is assumed that no crystallization occurs until the induction integral reaches 1, which is implemented so that the crystallization sub-model receives only the temperature history from full induction onwards. This, of course, is not an elegant implementation, and it does not allow for melt effects, but is ultimately pragmatic as it is intended to investigate temperature histories in MEX characterized by a complex cooling from the melt.

The model was manually re-fitted to the average crystallization kinetics function from 6 individual DSC runs at 1, 5, 10, 15, and 20°C/min cooling rates form 360°C, respectively. The DSC enthalpy was integrated over cubic Hermite polynomial baselines allowing for tangential transitions into the DSC curves on either end of the crystallization peak. The modelling equations are not repeated here as they are available in the publication of Bentalib [10]. The integration over temperature histories is implemented with a simple forward Euler method using a timestep of 0.1 s, which resulted for a complex temperature history in a relative error of approximately 0.2% compared to a 0.001 s resolution.

4. Crystallization Model Description

4.1. Induction Model

The induction model with the underlying dataset is displayed in Figure 1. It is evident that the induction time fit matches the data when plotted over cooling rates. Similarly, the isothermal datapoints shown in green on the right-side figure are matched in temperature space. The discrepancy of transient datapoints with the fit in temperature space is to be expected because

induction accelerates with undercooling. Therefore, less induction is accumulated over a constant cooling rate down to any temperature compared to an isothermal hold at the same (final) temperature. The fitting parameters are $T_m^0 = 300.69$ °C, $t_m = 13978$ s, and $a = 1.6005$.

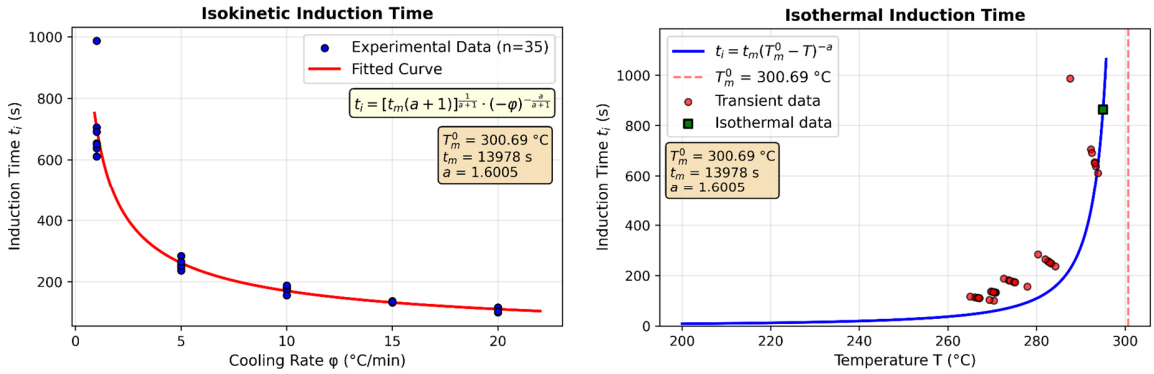

Figure 1. Non-isothermal induction time data and model fit over cooling rate (left) and temperature (right)

4.2. Crystallization Model Parameters

Sensitivity studies were conducted on all model parameters to assess the behaviour of relevant parameters, which were then fitted manually to DSC curves for cooling rates between 1 and 20 °C/min. The full set of parameters is not repeated here but is available in the publication of Bentalib et al. [10]. The adjusted parameters are the Ziabicki width parameter $D = 55.1$ K, the secondary Avrami-like exponent $n_s = 1.422$, and the maximum primary and secondary crystallinity of 0.174 and 0.09, respectively.

A rate sweep for constant cooling rates is presented in Figure 2, mapping out the model behaviour throughout the critical region of suppressed crystallization. It shows that the model is indeed capable of predicting both full crystallization and fully suppressed crystallization. The steep drop of the onset temperatures indicates that the induction is a major source for the suppression of crystallization at high rates. The prediction of induction approaching the glass transition may be flawed given that this approach neglects the nucleation-dominated effects for the sake of achieving the closed form solution.

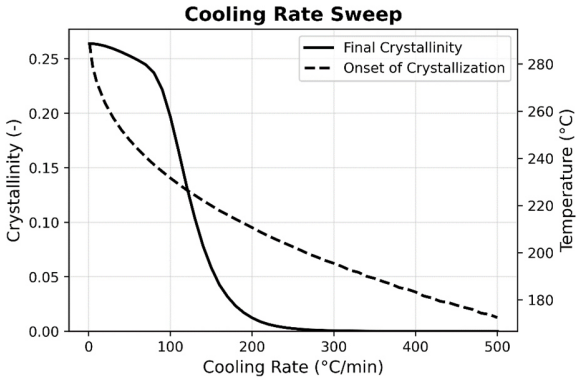

Figure 2. Rate sweep for the prediction of onset and final crystallinity in constant cooling ramps

4.3. Validation for Simple Temperature Histories

The model prediction for simple temperature histories at a constant cooling rate is presented in Figure 3 and compared to DSC-derived values. Each dashed line represents the average crystallization curve of 6 individual tests.

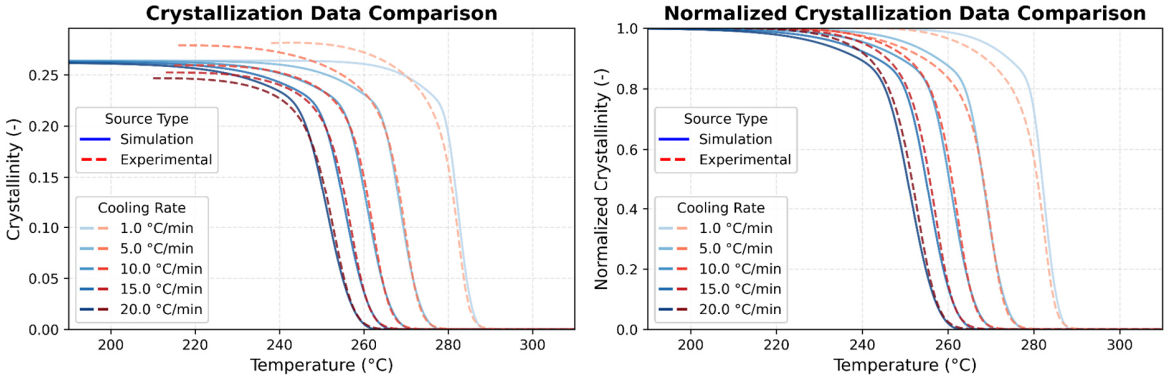

Figure 3. Model prediction and comparison to DSC test data for constant cooling rates in absolute (left) and normalized (right) crystallinity

The comparison of absolute values shows some discrepancy in the final crystallinity, which cannot be captured by the model. The prediction agrees well across both the absolute and normalized data, and particularly well in the onset and early growth region for all cooling rates.

5. Crystallization Modelling for Complex Temperature Histories

A representative IR image from the experimental validation is given in Figure 4. The printed structure on the lower end of the image exhibits a nearly one-dimensional temperature gradient in the vertical direction, with a particular warm (bright) region of newly deposited material trailing the nozzle. Time sequences were extracted from the warmest pixel immediately after deposition of the middle layer (25 out of 50) in the centre of the image. The resulting temperature profiles and corresponding predictions of induction and crystallization are displayed in Figure 5. The quasi-static temperature of material extrusion was determined to be 361°C based on the thermocouple measurements.

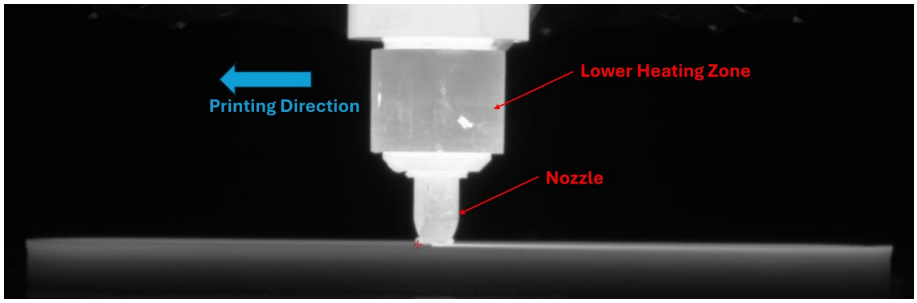

Figure 4. IR image of the print at 45 mm/s with a red marker indicating the pixel for which the time sequence was derived, in the moment prior to deposition

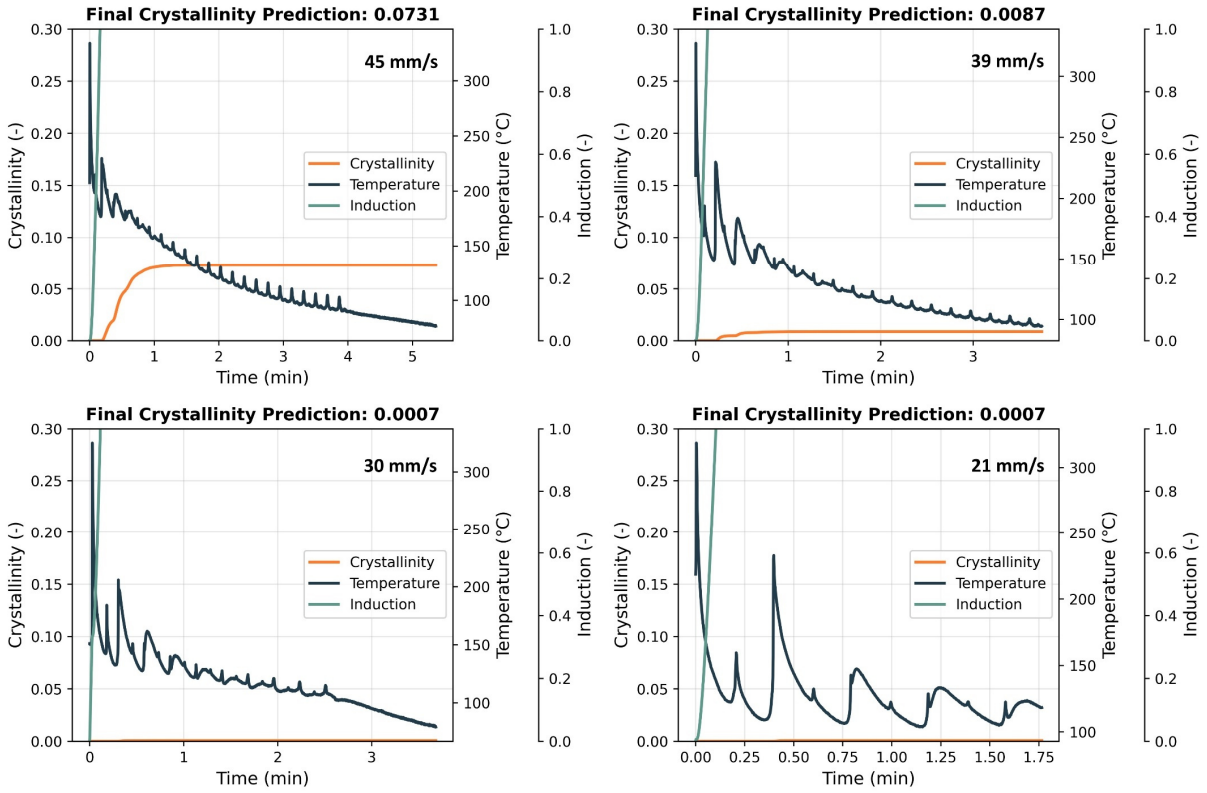

Figure 5. Temperature profiles with $\epsilon = 1.0$ and corresponding crystallinity simulations for printing speeds of 45, 39, 30 and 21 mm/s (left to right and top to bottom).

Examination of the temperature profiles above reveals two possible sources of errors. Firstly, the profiles exhibit a secondary peak in each cooling decay (seen most clearly for the 21 mm/s condition due to the scale), which is an effect of the hot nozzle passing through the background of the image while printing the far side of the part. The limited resolution results in radiation from the nozzle bleeding into the pixel from which the time sequence is derived. Secondly, the peak temperature values are significantly lower (319-335°C, ie ΔT = 26-42°C) than the extrusion temperature. This is likely an effect of the relatively low image resolution of 0.45 pixel per mm in conjunction with the high temperature gradients in vertical direction. The averaging of local temperatures in each pixel results in an underestimation of the local temperature. This could be countered by applying an apparent emissivity. A recalculation of temperatures following the Boltzmann law is done using equation (10), neglecting the effect of background radiation as a simplification.

$$T_{true} = T_{camera} \cdot \left(\frac{\epsilon_{true}}{\epsilon_{camera}}\right)^{-\frac{1}{4}} \tag{10}$$

The left plot in Figure 6 presents the results of the simulation with modified temperature profiles in a sweep over apparent emissivities between 0.75 and 1.0. The right side provides a comparison of the DSC-determined values for the final crystallinity. The predicted trend of decreasing crystallinity with decreasing print speed is captured well. However, a shift in absolute crystallinity values is also observed, particularly on the low end. A brief investigation was done with a set of

DSC tests of quenched material produced by extruding directly into water at ambient temperature, providing the highest achievable cooling rate in the available lab setting. The resulting average DSC crystallinity (average of 6 tests) was determined as 7.6%, well above the expected value of 0, and indeed close to the minimum values observed in Figure 6. This is in line with reports in the literature [16, 17] suggesting this enthalpy results from a large number of nuclei growing during quenching, rather than distinct crystallites, which is an effect not captured by the model.

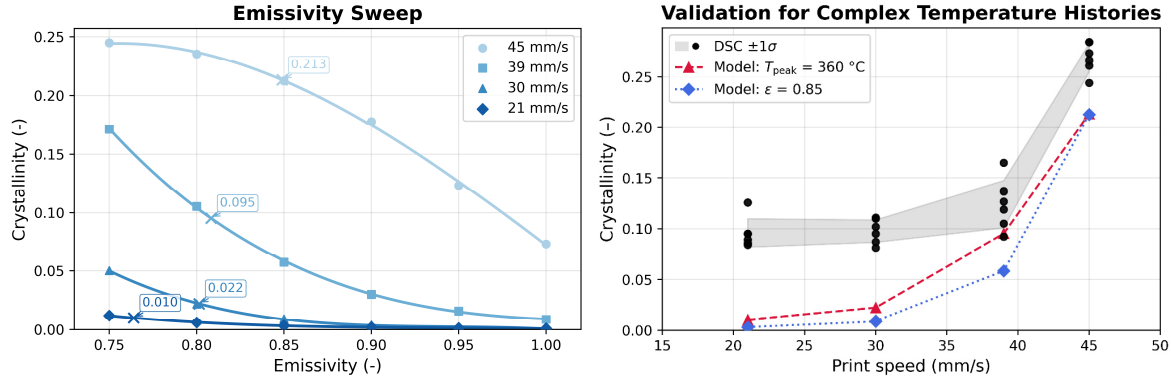

Figure 6. Left: Prediction of final crystallinity values for the temperature profiles modified with varying emissivity and annotation indicating the prediction for a peak temperature of 360°C, respectively. Right: Comparison of model prediction for constant peak temperature and constant emissivity with DSC tests.

6. Conclusion

In this work, a crystallization model for 30% short fibre reinforced LM-PAEK (231GRA) is presented, derived from a sophisticated Nakamura-based model for TC1225 reported in the literature and re-fitted to conventional DSC tests at cooling rates up to 20°C/min. The model was complemented with a new induction sub-model, for which a simplified method of fitting transient induction times from constant cooling rate tests to the closed form solution for the isokinetic induction integral was repurposed. The model prediction for low cooling rates is good. Complex temperature histories were derived from samples manufactured with FGF using an infrared camera. The model was able to capture the trend of decreasing final part crystallinity with increasing layer time, however, with an offset in the absolute crystallinity values compared to the DSC. The prediction was most sensitive to the choice of emissivity. Nevertheless, this method appears to be suitable for its intended use in studying the interaction of material and process parameters in additive manufacturing processes with complex temperature histories.

References

[1] R. Krueger und A. Bergan, „Advances in Thermoplastic Composites Over Three Decades–A Literature Review," *NASA STI Program Report Series; National Aeronautics and Space Administration: Washington, DC, USA,* 2024.

[2] C. M. S. Vicente, M. Sardinha, L. Reis, A. Ribeiro und M. Leite, „Large-format additive manufacturing of polymer extrusion-based deposition systems: review and applications," *Progress in Additive Manufacturing,* Bd. 8, p. 1257–1280, 2023.

[3] I. Mössinger, L. Raps, D. Fricke, J. Freund, M. Löbbecke und A. R. Chadwick, „Characteristics of in-situ automated fiber placement carbon-fiber-reinforced low-melt polyaryl ether ketone laminates part 1: Manufacturing influences," *Journal of Composite Materials,* Bd. 58, p. 1769–1787, 2024.

[4] T. J. Coogan und D. O. Kazmer, „Bond and part strength in fused deposition modeling," *Rapid Prototyping Journal,* Bd. 23, p. 414–422, 2017.

[5] X. Gao, S. Qi, X. Kuang, Y. Su, J. Li und D. Wang, „Fused filament fabrication of polymer materials: A review of interlayer bond," *Additive Manufacturing,* Bd. 37, p. 101658, 2021.

[6] P. Consul, A. Chaplin, N. Tagscherer, S. Zaremba und K. Drechsler, „Interlaminar strength in large-scale additive manufacturing of slow crystallizing polyaryletherketone carbon composites," *Polymer International,* Bd. 70, p. 1099–1108, 2021.

[7] T. J. Chapman, J. W. Gillespie Jr, R. B. Pipes, J.-A. E. Manson und J. C. Seferis, „Prediction of process-induced residual stresses in thermoplastic composites," *Journal of composite materials,* Bd. 24, p. 616–643, 1990.

[8] K. Nakamura, T. Watanabe, K. Katayama und T. S. Amano, „Some aspects of nonisothermal crystallization of polymers. I. Relationship between crystallization temperature, crystallinity, and cooling conditions," *Journal of Applied Polymer Science,* Bd. 16, p. 1077–1091, 1972.

[9] K. Gordnian, „Crystallization and thermo-viscoelastic modelling of polymer composites," 2017.

[10] S. Bentalib, M. van Drongelen, E. T. J. Klompen und F. Rondina, „Crystallization kinetics modelling of CF/LM-PAEK," in *SAMPE Europe Conference 2025 Amsterdam*, 2025.

[11] D. J. Blundell und B. N. Osborn, „The morphology of poly (aryl-ether-ether-ketone)," *Polymer,* Bd. 24, p. 953–958, 1983.

[12] C. L. Choy, K. W. Kwok, W. P. Leung und F. P. Lau, „Thermal conductivity of poly (ether ether ketone) and its short-fiber composites," *Journal of Polymer Science Part B: Polymer Physics,* Bd. 32, p. 1389–1397, 1994.

[13] T. L. Bergman und A. S. Lavine, Fundamentals of heat and mass transfer, 8 Hrsg., John Wiley & Sons, 2017.

[14] T. W. Chan und A. I. Isayev, „Quiescent polymer crystallization: modelling and measurements," *Polymer Engineering & Science,* Bd. 34, p. 461–471, 1994.

[15] W. L. Sifleet, N. Dinos und J. R. Collier, „Unsteady-state heat transfer in a crystallizing polymer," *Polymer Engineering & Science,* Bd. 13, p. 10–16, 1973.

[16] H. J. Zimmermann und K. Könnecke, „Crystallization of poly (aryl ether ketones): 3. The crystal structure of poly (ether ether ketone ketone)(PEEKK)," *Polymer,* Bd. 32, p. 3162–3169, 1991.

[17] J. D. Hoffman und J. I. Lauritzen Jr, „Crystallization of bulk polymers with chain folding: theory of growth of lamellar spherulites," *Journal of research of the National Bureau of Standards. Section A, Physics and chemistry,* Bd. 65, p. 297, 1961.